GLOBAL BIOGEOCHEMICAL CYCLES, VOL. 15, No. 2, PAGES 467-481, JUNE 2001

Modeling the variation of $\delta^{13}C$ in atmospheric methane: Phase ellipses and the kinetic isotope effect

W. Allan, M. R. Manning, K. R. Lassey, D. C. Lowe, and A. J. Gomez

National Institute of Water and Atmospheric Research, Wellington, New Zealand

Abstract. We use the TM2 three-dimensional atmospheric tracer model with a methane source-sink budget based on existing literature to simulate small spatial and temporal variations in the $^{13}C/^{12}C$ ratio of atmospheric methane. The results show that $\delta^{13}C$ varies markedly with wind direction everywhere outside the extratropical Southern Hemisphere (ETSH). Within the ETSH, both methane mixing ratio and $\delta^{13}C$ have regular seasonal cycles with differing and latitude-dependent phases. Phase diagrams constructed from these seasonal cycles, showing changes in $\delta^{13}C$ versus changes in mixing ratio, have elliptical shapes. The slope of the major axis of these ellipses is determined by the kinetic isotope effect (KIE) of the single atmospheric methane removal process used in the model. The ellipse eccentricity is determined by seasonal variation in the source $\delta^{13}CH_4$, which is dominated by the biomass burning source because of its isotopic enrichment relative to other sources. Comparison of the model results, for a KIE based on CH_4 + OH oxidation, with observations in the South Pacific region shows significant discrepancies in both the ellipse major axis slopes and eccentricities. We suggest that this is an indicator of an additional sink process that discriminates strongly against $^{13}CH_4$. Such a sink could be active chlorine in the marine boundary layer.

1. Introduction

The atmospheric burden of methane (CH_4) has more than doubled in the last 150 years [*Etheridge et al.*, 1998]. Almost all of this increase can be attributed to growing anthropogenic methane sources. Because methane absorbs infrared radiation, it plays an important part in Earth's atmospheric radiation balance and is responsible for a significant fraction of anthropogenic climate forcing due to greenhouse gases [e.g., *Crutzen*, 1995]. Methane also plays a significant role in tropospheric chemistry, where it is a major regulator of the hydroxyl radical (OH) and a source of hydrogen and carbon monoxide. Methane oxidation in the stratosphere produces water vapor which modifies both radiative energy balance and stratospheric chemistry.

A fairly consistent picture of the global methane budget has been developed by fitting the output of various transport and chemistry models to mixing ratio observations made over several years at a number of sites in the northern hemisphere (NH) and southern hemisphere (SH) [e.g., *Fung et al.*, 1991; *Hein et al.*, 1997]. Variations in the isotopic composition of atmospheric methane can provide further constraints on the global methane budget because several source types can be distinguished by their characteristic isotope signatures. For example, methanogenesis under anaerobic conditions results in methane that is relatively depleted in ^{13}C, while methane released in biomass burning is relatively enriched in ^{13}C [*Stevens and Engelkemeir*, 1988].

For methane, $^{13}C/^{12}C$ isotopic ratios are reported through the $\delta^{13}C$ ratio defined by

$$\delta^{13}C \equiv \frac{[^{13}CH_4]/[^{12}CH_4]}{R_0} - 1, \qquad (1)$$

where $R_0 = (^{13}C/^{12}C)_{PDB}$ has an accepted value of 0.0112372 for the isotope standard, peedee belemnite (PDB) [*Craig*, 1957]. Usually, $\delta^{13}C$ is scaled by a factor of 1000 and reported as per mill "*‰*." For compactness we refer to the $\delta^{13}C$ of the carbon in methane as "$\delta^{13}CH_4$."

To date, stable carbon isotope signatures have not been used widely in modeling the structure of atmospheric methane in space and time. *Fung et al.* [1991] showed that the mean value of $\delta^{13}CH_4$ imposed a constraint on the relative mix of isotopically light and heavy sources. *Hein et al.* [1997] considered site-

Paper number 2000GB001282.
0886-6236/01/2000GB001282$12.00

specific data on $\delta^{13}CH_4$ in their three-dimensional inverse modeling of the global methane budget. *Gupta et al.* [1996] considered isotopic fractionation effects of several methane sinks in a two-dimensional model. Our purpose in the present work is to investigate the detailed structure of the $\delta^{13}CH_4$ signature in atmospheric methane as predicted using a three-dimensional transport model. In particular, we address model simulation of $\delta^{13}CH_4$ seasonal cycles in the extratropical Southern Hemisphere (ETSH) and compare with observations in that region. We demonstrate that the ETSH provides a natural laboratory for examining the methane cycle in a sink-dominated region and that an integrated analysis of seasonal data there provides an assessment of the sink-induced isotopic fractionation. Note that the molar mixing ratio, defined as moles of methane per mole of dry air, is referred to many times in this paper, and we will use the abbreviation "MR."

2. Model

We use the three-dimensional transport model TM2 [*Heimann*, 1995] to deduce spatial and temporal patterns of atmospheric methane and its carbon isotope components in steady state with prescribed methane source patterns. The model solves the continuity equation for atmospheric tracers on an Eulerian grid spanning the entire globe, calculating the source and sink processes affecting each tracer, followed by transport processes, at intervals of 4 hours. A model intercomparison [*Denning et al.*, 1999] has shown that TM2 performs reasonably well in predicting the global transport of the inert tracer SF_6, though all the models considered have imperfections. We employ transport fields based on 12-hourly meteorological analyses from the European Centre for Medium-Range Weather Forecasts (ECMWF) and apply these repetitively for each simulation year. These fields are interpolated onto the grid (7.8° latitude by 10° longitude and a sigma coordinate system with nine vertical layers) as described by *Heimann and Keeling* [1989] and *Heimann* [1995]. We use ECMWF analyses for 1987 as representative annual wind patterns, which should be adequate for predicting the general features of methane spatial and temporal structure.

Some global methane modeling studies have applied the constraint that the $\delta^{13}CH_4$ in the aggregate global source should match that observed in the atmosphere, adjusted for sink fractionation [e.g., *Fung et al.*, 1991]. This constrains the average global source value to near $-52‰$ as long as the global mean sink fractionation is near the value measured for the dominant OH sink by *Cantrell et al.* [1990]. As yet, space and time variations in atmospheric $\delta^{13}CH_4$ have not played a large role in contributing to an understanding of methane budgets and their validation, in part because of the dearth of isotopic measurements [e.g., *Quay et al.*, 1991; *Lowe et al.*, 1994, 1997; *Hein et al.*, 1997; *Bergamaschi et al.*, 2000]. *Hein et al.* [1997] derived spatiotemporal $\delta^{13}CH_4$ fields directly from an approximate weighted sum of their computed MR fields.

2.1. Treatment of Sources and Sinks

We employ eleven different source categories each with geographic and time variation as used by *Fung et al.* [1991], interpolated onto the TM2 grid. The categories are shown in Table 1, with $\delta^{13}C$ values selected as being representative within the constraint of a global mean value near $-52‰$. Only the two wetlands sources, the rice source, and the biomass burning source are taken to vary seasonally, with all other sources aseasonal. *Fung et al.* [1991, Table 4] show that the latitudinal distributions of all sources are weighted to a greater or lesser extent toward the NH, except for the swamps/alluvial source, which has a moderate weighting toward the SH. While the geographical and seasonal variations of sources adopted for this work are those of *Fung et al.* [1991], we apply individual source strengths (Table 1) tuned to more recent budget analyses [e.g., *Prather et al.*, 1995; *Francey et al.*, 1999]. The total source strength of 590 Tg yr^{-1} is consistent with recent Intergovernmental Panel on Climate Change (IPCC) assessments [*Schimel et al.*, 1996]. The methane budget in Table 1 was recently shown by *Lowe et al.* [1999] to provide a reasonably accurate simulation of methane MR and $\delta^{13}CH_4$ observations made on ship transits

Table 1. A Global Methane Source Budget Modified From *Francey et al.* [1999] and *Lassey et al.* [2000] based on IPCC source strengths [*Prather et al.*, 1995; *Schimel et al.*, 1996][a]

Source Type	Strength, Tg CH_4 yr^{-1}	$\delta^{13}CH_4$, ‰
Animals	125	−63
Wetlands[b]		
bogs/tundra	45	−64
swamps/alluvial	95	−59
Rice[b]	65	−62
Landfills	65	−51
Natural gas vents	20	−40
Natural gas leaks	65	−40
Coal mining	45	−38
Biomass burning[b]	45	−25
Termites	20	−62
Total	590	−52.9[c]
Soil absorption	−30	−69
Total	560	−52.0[c]

[a]The $\delta^{13}CH_4$ values are based on *Hein et al.* [1997], *Francey et al.* [1999], and *Lassey et al.* [2000]. The soil absorption sink is included as a negative source with a $\delta^{13}CH_4$ value in the removed flux given by the atmospheric value ($-47‰$) adjusted due to fractionation by $-22‰$ (see text for details).

[b]Seasonally varying sources.

[c]Weighted mean.

across the Pacific over a wide latitude range. Following *Fung et al.* [1991], we include soil absorption as an effective negative source with strength -30 Tg yr^{-1} and associate with it an effective $\delta^{13}C$ value of $-69‰$. This provides a sink flux fractionated by $-22‰$ relative to an atmosphere of $-47‰$, consistent with measurements [*Tyler et al.*, 1994; *Snover and Quay*, 2000].

Methane is destroyed mainly by tropospheric OH, and we follow *Fung et al.* [1991] in using the space and time varying OH fields calculated by *Spivakovsky et al.* [1990] as the sole atmospheric sink. The OH loss rate of methane in the TM2 model is

$$\text{Loss rate} = k[\text{OH}][\text{CH}_4], \quad (2)$$

where the brackets denote the corresponding concentration and k is a temperature-dependent rate coefficient given by *DeMore et al.* [1997]. Since this is effectively the rate coefficient for $^{12}CH_4$, we refer to it as k_{12}. The removal of $^{13}CH_4$ by OH is slightly slower than for $^{12}CH_4$ (i.e., $k_{13} < k_{12}$), an effect known as isotope fractionation. We adopt the value $(k_{13}/k_{12})_{OH} = 0.9946$ [*Cantrell et al.*, 1990]. Defining $\epsilon = (k_{13}/k_{12}) - 1$ as the "kinetic isotope effect" or KIE, we therefore adopt $\epsilon_{OH} = -0.0054$ (or $-5.4‰$) for the CH_4 + OH reaction.

The OH field derived by *Spivakovsky et al.* [1990] gives an atmospheric CH_4 + OH lifetime longer than the 9 years suggested by *Prinn et al.* [1995]. We account for this by including a numerical factor of 1.278 multiplying k[OH] in (2), thus strengthening the sink and decreasing the lifetime to 9 years. This factor would increase the global tropospheric mean OH concentration from $8 \cdot 10^5$ cm^{-3} for the OH fields of *Spivakovsky et al.* [1990] to agree more closely with the value $(9.7 \pm 0.6) \cdot 10^5$ cm^{-3} deduced by *Prinn et al.* [1995] for the 1990s to account for CH_3CCl_3 observations.

The OH field of *Spivakovsky et al.* [1990] is derived externally and may not be fully self-consistent with the methane source structure adopted here. However, recent modeling studies show that fine details of the OH distribution used do not appreciably affect the modeled structure of long-lived atmospheric species. *Houweling et al.* [1998] used two very different OH fields to model the distribution of CH_3CCl_3 (with a lifetime of the same order as methane) and found only very small differences in the modeled structure of the CH_3CCl_3. We therefore consider that lack of self-consistency (or feedback) between source and sink distributions does not significantly affect our results.

2.2. Building Block Approach

We adopt a "building block" approach to the methane budget, similar to that employed by *Fung et al.* [1991]. Each building block is a spatial and seasonal distribution of MR at equilibrium, derived from prescribed distributions in both space and time of a single source category normalized to unit strength. The model is run separately for each source category in Table 1 (including the negative soil source), initialized with our best estimate of the final global mean equilibrium MR for that source (to reduce "spin-up" time), and using the rate coefficient k_{12}. Each run is for 50 model years to ensure that a steady state of source/sink driven variations develops, and we take as the building block the MR for $^{12}CH_4$ in the last year. The complete MR structure is synthesized as a weighted sum of the building blocks, using the source strengths in Table 1 as weights.

To obtain the space and time variation of $\delta^{13}CH_4$, we derive a companion set of building blocks for $^{13}CH_4$ as for $^{12}CH_4$ but with rate coefficient k_{13}. Because $\delta^{13}CH_4$ reaches equilibrium much more slowly than MR [*Tans*, 1997; *Lassey et al.*, 2000], the model runs used here are significantly longer than used in previous methane modeling work. Year to year variations in $\delta^{13}CH_4$ at the end of these runs are typically $< 0.01‰$, indicating that a steady state has been reached and that temporal variations larger than this are not the result of numerical inaccuracy.

As a more detailed description of the synthesis process, suppose there is a given methane emission inventory E, in which there are n source categories with strengths S_i $(i = 1 \ldots n)$ and $\delta^{13}C$ values δ_i. Now, $S_i = {}^{12}S_i + {}^{13}S_i$ and ${}^{13}S_i = R_0\,{}^{12}S_i\,(1 + \delta_i)$, where ${}^{12}S_i$ and ${}^{13}S_i$ are the ^{12}C and ^{13}C components of the sources in Tg yr^{-1}. Let us denote the $^{12}CH_4$ building blocks by ${}^{12}B_i$ and the $^{13}CH_4$ building blocks by ${}^{13}B_i$. Then the synthesized atmospheric MR distribution is

$$\begin{aligned}[\text{CH}_4]_E &= [{}^{12}\text{CH}_4]_E + [{}^{13}\text{CH}_4]_E \\ &= \sum_{i=1}^{n} ({}^{12}B_i\,{}^{12}S_i + {}^{13}B_i\,{}^{13}S_i).\end{aligned}$$

If we write ${}^{13}B_i = (1 + e_i)\,{}^{12}B_i$, then the values e_i are nonzero due to the combined effects of transport and the slower removal rate for $^{13}CH_4$ and are of the order of the KIE (ϵ). The methane MR can then be written as

$$[\text{CH}_4]_E = \sum_{i=1}^{n} {}^{12}B_i S_i + R_0 \sum_{i=1}^{n} e_i\,{}^{12}B_i(1 + \delta_i)\,{}^{12}S_i, \quad (3)$$

where the second term on the right is of order $R_0\epsilon$ and can generally be ignored relative to the first term.

From (1), the corresponding synthesized atmospheric $\delta^{13}C$ is

$$\begin{aligned}(\delta^{13}\text{CH}_4)_E &= \frac{\sum_{i=1}^{n} {}^{13}B_i\,{}^{13}S_i}{R_0 \sum_{i=1}^{n} {}^{12}B_i\,{}^{12}S_i} - 1 \\ &= \frac{\sum_{i=1}^{n} {}^{13}B_i\,{}^{12}S_i\,(1 + \delta_i)}{\sum_{i=1}^{n} {}^{12}B_i\,{}^{12}S_i} - 1 \quad (4)\end{aligned}$$

$$
\begin{aligned}
(\delta^{13}\mathrm{CH_4})_E &= \frac{\sum_{i=1}^{n}({}^{13}B_i - {}^{12}B_i)\,{}^{12}S_i}{\sum_{i=1}^{n}{}^{12}B_i\,{}^{12}S_i} \\
&\quad + \frac{\sum_{i=1}^{n}{}^{13}B_i\,{}^{12}S_i\delta_i}{\sum_{i=1}^{n}{}^{12}B_i\,{}^{12}S_i} \\
&= \frac{\sum_{i=1}^{n}{}^{12}B_i\,{}^{12}S_i e_i}{\sum_{i=1}^{n}{}^{12}B_i\,{}^{12}S_i} \\
&\quad + \frac{\sum_{i=1}^{n}{}^{13}B_i\,{}^{12}S_i\delta_i}{\sum_{i=1}^{n}{}^{12}B_i\,{}^{12}S_i}. \qquad (5)
\end{aligned}
$$

The first and second terms on the right-hand side of (5) are the contributions from sink fractionation and from sources, respectively. If the sources S_i were aseasonal and the methane lifetime were sufficiently long relative to atmospheric mixing times that the atmosphere could be treated as a well-mixed box, then the building blocks ${}^{12}B_i$ and ${}^{13}B_i$ would be constant everywhere, independent of the source distribution, and proportional to the $^{12}CH_4$ and $^{13}CH_4$ lifetimes. In this idealized case, $(1+e_i) = (1+\epsilon)^{-1}$ for all S_i and (5) simplifies to

$$(\delta^{13}\mathrm{CH_4})_E \approx -\epsilon/\alpha + \bar{\delta}/\alpha, \qquad (6)$$

where $\alpha = 1+\epsilon$ is the fractionation factor. The two terms in (6) correspond to their counterparts in (5). The first term in (6) is the shift due to fractionation that adjusts the $\delta^{13}CH_4$ value in the mean source, $\bar{\delta}$, to that found in atmospheric methane [e.g., *Lassey et al.*, 2000]. Expression (6) is usually further simplified with the first-order substitution $\alpha \simeq 1$ [e.g., *Stevens and Engelkemeir*, 1988; *Fung et al.*, 1991].

For the more general case (5), fractionation introduces extra space and time variation into $(\delta^{13}CH_4)_E$ because of the differences between the 4-dimensional fields ${}^{13}B_i$ and ${}^{12}B_i$. Thus (5) specifies more accurately the ^{13}C-enrichment as source methane is redistributed to atmospheric methane. It is implicit in (5) that as the methane ages it becomes isotopically heavier, so that regions furthest from sources generally see the heaviest methane. A consequence of this is the isotopically heavier methane in the SH compared to the NH [e.g., *Lowe et al.*, 1999]. To a good approximation, we can replace ${}^{12}S_i$ by S_i in (4), and we use this form in the model. The errors incurred are of order $R_0\Delta\delta_i$, where $\Delta\delta_i$ are fluctuations in the source $\delta^{13}CH_4$ values about $\bar{\delta}$.

To aid in interpreting later results, consider the relationship between small changes in δ^{13}C and changes in MR. As derived in the appendix, this can be expressed as

$$\Delta\delta \approx \epsilon(1+\delta_0)\Delta C/C_0, \qquad (7)$$

which relates variations in atmospheric $\delta^{13}CH_4$ values $\Delta\delta$ about the mean value δ_0 to relative MR variations $\Delta C/C_0$, over a relatively short time interval (say 1 year), C_0 being the mean MR over the interval. If we plot $\Delta\delta$ versus $\Delta C/C_0$ over such a time interval, we obtain the "kinetic isotope effect (or KIE) line" of slope $\epsilon(1+\delta_0)$. Expression (7) strictly applies to a closed box, and if observations were available for such a closed box, the KIE ϵ could be derived from the measured slope of the KIE line. We argue below that the ETSH atmosphere has features in common with such a box.

3. Results

The building blocks were combined as discussed in section 2 for the methane budget in Table 1. The result is a 4-dimensional array for methane MR obtained from (3) and for δ^{13}C obtained from (4). Each array contains values for 36 cells in longitude by 24 cells in latitude by 9 heights, for each of 365 daily means of the final year of the run. All results described below are for the surface layer (0 – 360 m height).

The observed atmosphere is not in equilibrium. As an empirical adjustment, we have used the results of *Lassey et al.* [2000], who estimate the evolving extent of disequilibrium based on a simple global model. We adjust each simulated MR time series by −45 ppb and each simulated $\delta^{13}CH_4$ time series by −0.38‰, as appropriate for 1997 [*Lassey et al.*, 2000, Figure 3]. Note that the latter adjustment would be different if the global KIE were taken as other than −5.4‰. The adjusted 4-dimensional model fields determined in this way have SH MR and $\delta^{13}CH_4$ averages of 1695 ppb and −47.18‰ and NH averages of 1804 ppb and −47.40‰. The same model outputs were used by *Lowe et al.* [1999] to compare with their Pacific ship transit observations. *Lowe et al.* [1999, Figures 2 and 4] show that the model gives good qualitative agreement with the observed interhemispheric differences but that NH MR values are somewhat overestimated in the model. Yearly mean adjusted model values of MR and δ^{13}C at SH midlatitude positions shown later are consistent with observations in the New Zealand region in the middle of the 1990-1996 time period, as given by *Lowe et al.* [1997]. Although the methane budget developed in this paper is not optimized, it is appropriate to test the detailed $\delta^{13}CH_4$ variations produced by the TM2 model in the ETSH.

Figures 1, 2, and 3 illustrate the model results at three latitudes in each hemisphere along the 180° meridian. The cell with center latitude −74.3° contains the National Institute of Water and Atmospheric Research (NIWA) observing station at Scott Base, Antarctica (−77.8°), and the −43.0° cell contains the NIWA station at Baring Head, New Zealand (−41.4°). The cell with center latitude −11.7° was chosen to illustrate differences between ETSH and tropical SH results. The corresponding northern latitudes are shown to illustrate hemispheric differences. Note that all displayed locations are at oceanic or sea ice sites, and axis scales at the bottom of Figures 1, 2, and 3 are the same to highlight the interhemispheric differences. The time series of MR and $\delta^{13}CH_4$ shown in Figures 1, 2, and 3 have variations on a synoptic timescale. We interpret these

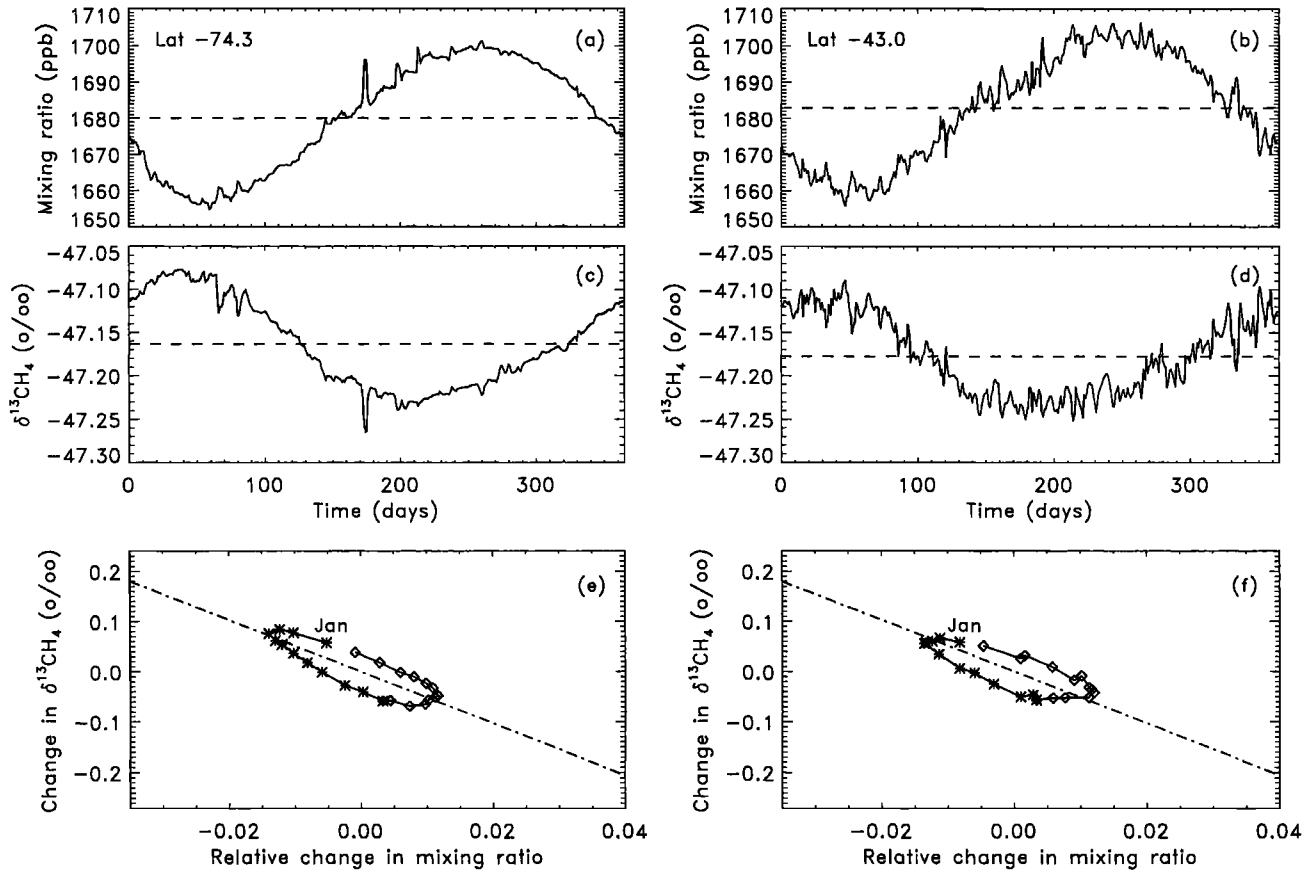

Figure 1. Temporal variations of modeled mixing ratio and $\delta^{13}CH_4$ in the TM2 cells with central latitudes −74.3° and −43.0° in the extratropical Southern Hemisphere. (a)–(d) The dashed lines give the yearly mean values. Day 1 is January 1 in each case. (e)–(f) The corresponding phase diagrams with two-weekly average values marked by asterisks for the first six months of the year (with January marked) and by diamonds for the last six months of the year are shown. The dash-dot line is the "KIE line" of (7) for the KIE used in the model (−5.4‰). Note that the MR time series has been adjusted for disequilibrium by −45 ppb and the $\delta^{13}CH_4$ by −0.38‰ as discussed in the text.

variations as being caused by synoptic-scale wind shifts that move air with differing values of MR and $\delta^{13}CH_4$ into and out of a given computational cell.

Figure 1 shows the model results for the two positions in the ETSH. Figure 1a displays the MR time series for latitude −74.3°, which has the expected reasonably smooth seasonal variation with evidence for an occasional intrusion of air from lower latitudes (the relatively large "spikes"). The $\delta^{13}CH_4$ time series in Figure 1c also shows a smooth seasonal variation and indicates that the intrusions from lower latitudes are relatively depleted in $^{13}CH_4$.

Figure 1e shows the "phase diagram" obtained when the change in $\delta^{13}CH_4$ is plotted versus the change in MR relative to the yearly mean MR. A similar technique for displaying the relationship between MR and isotopic ratio changes has been used for other atmospheric species [e.g., *Keeling et al.*, 1989]. The phase shift between MR and $\delta^{13}CH_4$ cycles results in a tilted ellipse-like shape, which we will term the "phase ellipse." Equation (7) with $\epsilon = -0.0054$ and δ_0 equal to the yearly mean $\delta^{13}CH_4$ gives the dashed-dotted line, the KIE line discussed earlier, and represents the major axis of the ellipse well. These results are typical of all longitudes at this latitude.

Figures 1b, 1d, and 1f show corresponding results for the cell with center latitude −43.0°, containing the Baring Head station. The phase ellipse in Figure 1f is similar, with the January position changed between the two latitudes. The ellipse at −43.0° is typical of results at all longitudes at this latitude except those in the Atlantic to the east of South America, which are much more irregular.

The results in Figures 2a, 2c, and 2e for the cell with center latitude −11.7° (N of Fiji) are interesting. From about the end of May until mid-December the MR shows a seasonal structure similar to more southerly latitudes. However, from mid-December to mid-May

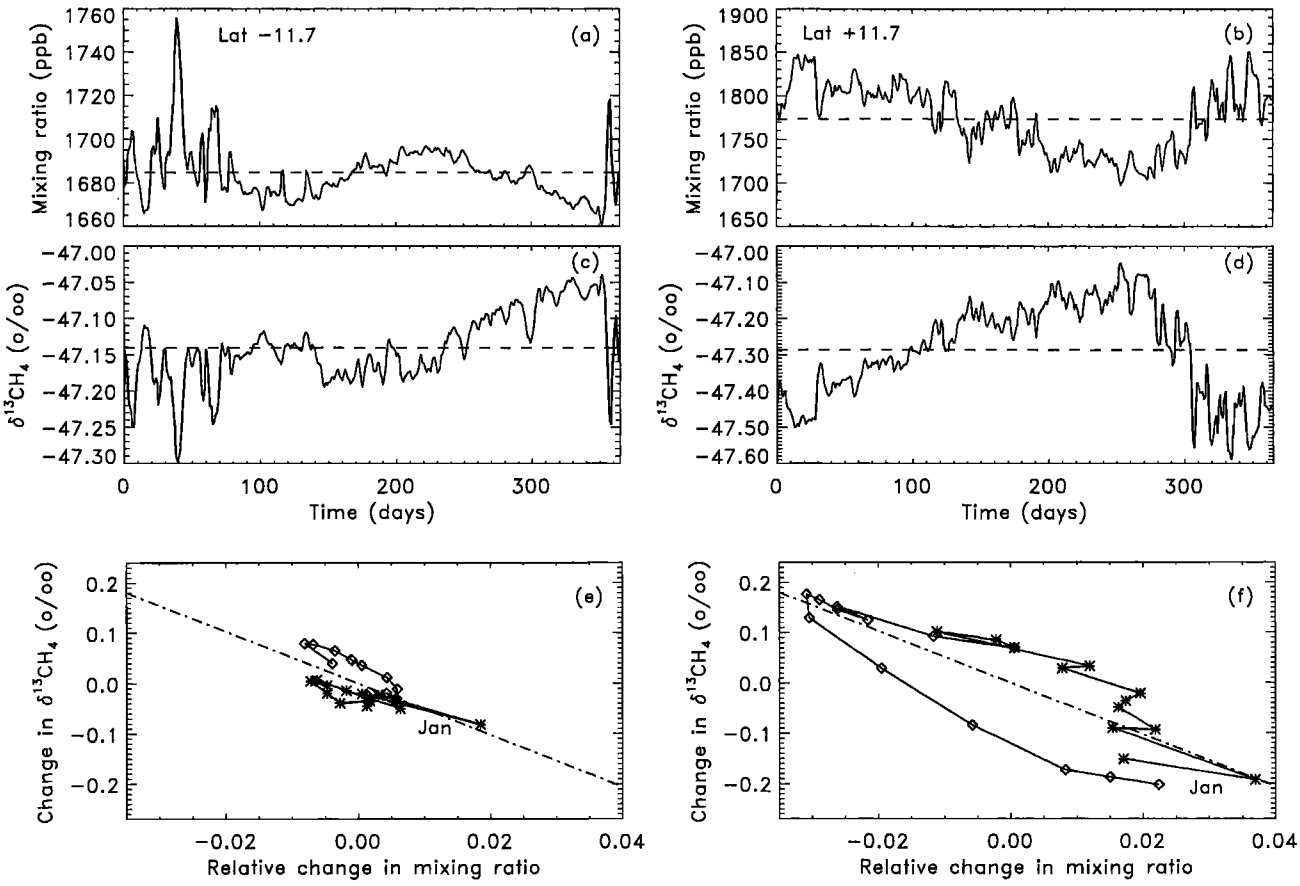

Figure 2. As Figure 1, for latitudes −11.7° and +11.7° in the southern and northern tropics respectively, with axis scales in Figures 2e and 2f identical to those of Figure 1.

there are large-amplitude, rapid fluctuations. These are mirrored in the $\delta^{13}CH_4$ time series in which $\delta^{13}CH_4$ decreases as MR increases. The seasonal behavior seen at these times in more southerly latitudes is destroyed by these fluctuations and results in a very irregular phase diagram as shown in Figure 2e. An explanation for this can be found in the equivalent NH results in Figures 2b, 2d, and 2f (at an ocean site east of the Marshall Islands). At latitude +11.7°, both MR and $\delta^{13}CH_4$ have opposite phase and large, irregular amplitudes compared with the southerly latitudes in Figure 1 and with the −11.7° results after the end of May. It is reasonable to propose that NH air intrudes to southern low latitudes from mid-December to mid-May. Two-dimensional animations of the MR and $\delta^{13}CH_4$ patterns confirm this interpretation. The transition to much larger variations in both MR and $\delta^{13}CH_4$ in the NH is clearly seen by comparing the phase diagrams in Figure 2.

Figure 3 shows results for extratropical Northern Hemisphere latitudes corresponding to the southern latitudes in Figure 1. The NH time series (at an ocean site east of Japan and at a site in the Arctic Ocean) are much more variable on short timescales, and the $\delta^{13}CH_4$ seasonal cycles have significantly larger amplitudes than in the SH. The phase diagrams are irregular (particularly for +74.3°) and are not related to the KIE line. At this latitude, frequent short-term MR variations punctuate any smooth seasonal variation, to the point where the latter is barely discernible. We believe that such gross distortions of the ellipses are due largely to the effect of many local sources of different origin combining to deliver methane that has strongly varying MR and $\delta^{13}C$ signatures.

Note that the temporal variability of both MR and $\delta^{13}CH_4$ in Figures 1, 2, and 3 is comparable with that in the observations of *Quay et al.* [1991, 1999] and *Lowe et al.* [1994, 1997], although the observations were generally not made on the 1-day timescale of the simulation. The results in Figure 3 for northern temperate and polar latitudes show that source and atmospheric transport effects are important in determining seasonal variations in these regions, as discussed by *Quay et al.* [1999]. However, the results in Figure 2 show that transport effects are also significant for a large part of the year at tropical latitudes.

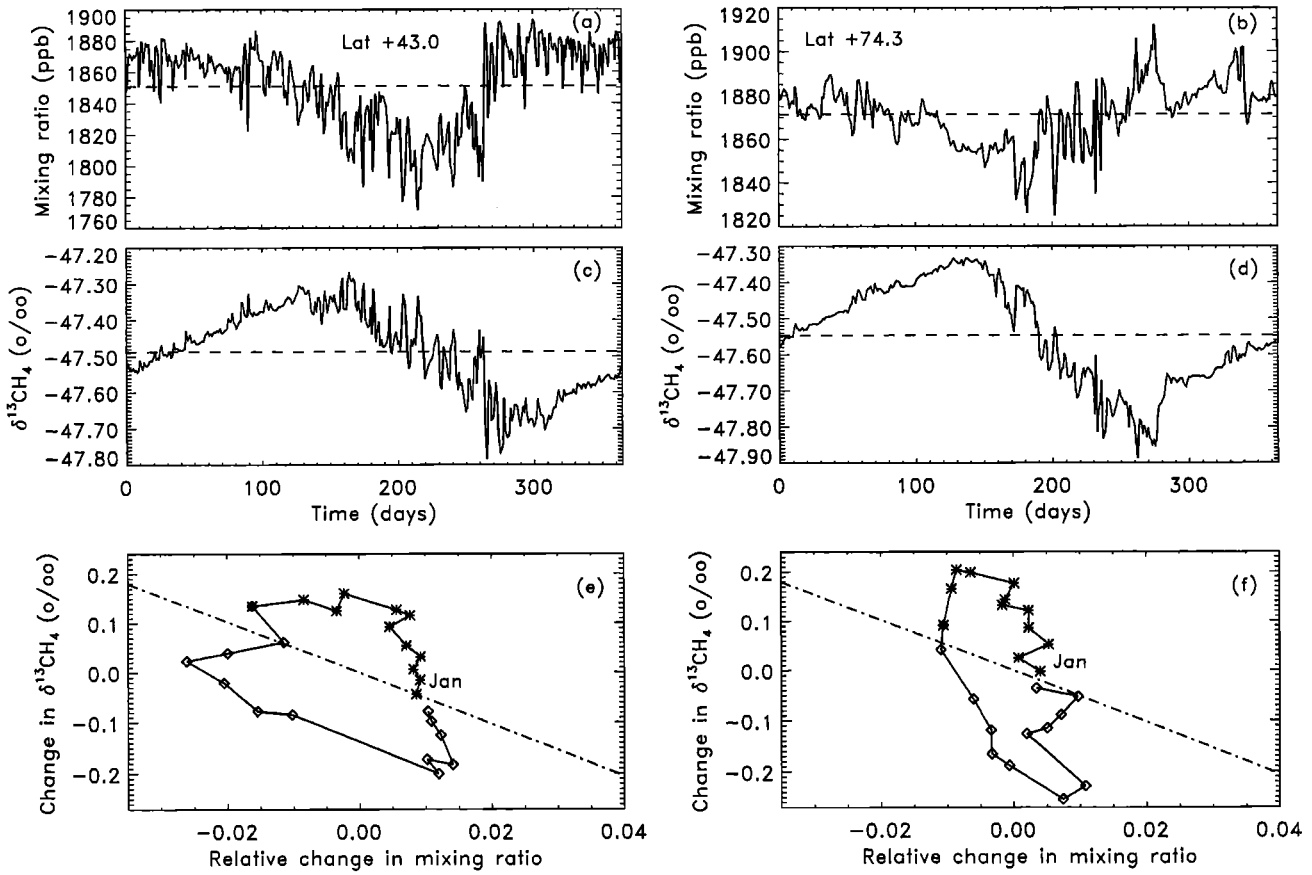

Figure 3. As Figure 1, for latitudes +43.0° and +74.3° in the extratropical Northern Hemisphere, with axis scales in Figures 3e and 3f identical to those of Figures 1 and 2.

4. Phase Ellipse Properties

The phase ellipses discussed in section 3 do not contain any more information than the MR and $\delta^{13}CH_4$ time series used to create them. However, they provide a distillation of the properties of the time series amenable to visual assimilation.

4.1. Length of Ellipse Major Axis

The most obvious ellipse property is the length of the major axis, which is essentially the relative peak-to-trough amplitude of the MR seasonal cycle. In the ETSH this amplitude is principally determined by the OH seasonal cycle amplitude, as explained by *Lassey et al.* [1993]. Results described in section 4.4 for a modified OH field further demonstrate this property.

4.2. January Position and Rotation Sense

The January position is determined by the phases of the seasonal cycles. In what follows we derive amplitude (A) and phase (ϕ) values from least squares fits of the function $A\sin(\omega t + \phi)$ to either the MR or the $\delta^{13}CH_4$ time series on the basis that these fits represent the time series well in the ETSH. Time t is measured from January 1, and frequency ω corresponds to a seasonal cycle. Figure 4 shows the phases ϕ_{MR} and ϕ_{DC} of the MR and $\delta^{13}CH_4$ cycles versus latitude in the ETSH. The latitudinal gradients of both phases show that the MR and $\delta^{13}CH_4$ fields have spatial structures that propagate toward the south pole. The MR structure propagates at ~3° of latitude per day, somewhat faster than the $\delta^{13}CH_4$ structure, which propagates at ~2° per day. These values imply that it takes ~20 days for changes in MR to propagate from the southern equatorial region to the south polar region and ~30 days for changes in $\delta^{13}CH_4$ to reach the south polar region. A visual indicator of this faster propagation of MR compared to $\delta^{13}CH_4$ is the clockwise rotation of the January position around the ellipse as the latitude moves poleward (Figure 1). This change with latitude is distinct from the anticlockwise rotation sense of the ellipse at a given latitude, which results from the peak of $\delta^{13}CH_4$ leading the trough of MR (Figure 1). Also shown in Figure 4 is $\Delta\phi = \phi_{MR} - \phi_{DC}$, which is discussed below.

4.3. Ellipse Eccentricity

The ellipse eccentricity, ideally given by $(1-b^2/a^2)^{1/2}$ where b and a are the lengths of the semiminor and

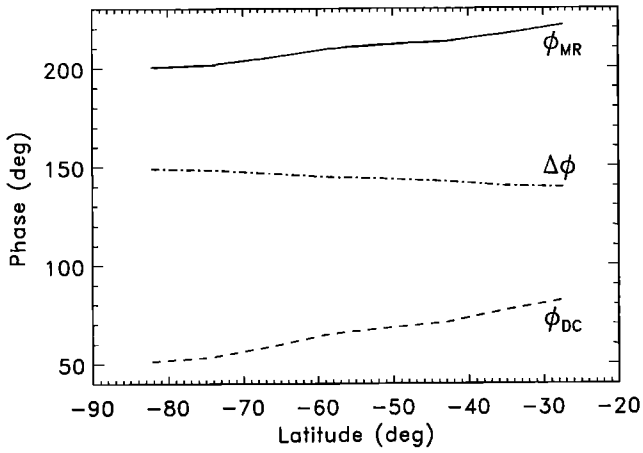

Figure 4. Modeled variation with latitude of the MR phase ϕ_{MR} (solid line), the $\delta^{13}CH_4$ phase ϕ_{DC} (dashed line), and the phase difference $\Delta\phi$ between them (dashed-dotted line) for the ETSH.

semimajor axes, respectively, indicates visually the phase difference ($\Delta\phi$) between the MR and $\delta^{13}CH_4$ cycles. When idealized sinusoidal MR and $\delta^{13}CH_4$ cycles are 180° out of phase ($\Delta\phi = 180°$), the ellipse becomes a straight line with negative slope and unit eccentricity. As $\Delta\phi$ decreases or increases away from 180°, the eccentricity declines as the ellipse minor axis enlarges, approaching zero eccentricity as the ellipse becomes a circle ($\Delta\phi = 90°$ or 270°). At $\Delta\phi = 0$ the ellipse would be a straight line with positive slope. As shown in Figure 4, $\Delta\phi$ increases from 139° at −27.4° latitude to 149° at −82.2° latitude, giving a relatively small increase in eccentricity with increasing southern latitude in the ETSH. Note that 1° of phase difference is approximately one day in time.

The ellipse eccentricity is strongly affected by the amplitude of the seasonal cycle in the biomass burning source. Figure 5 shows the ellipses obtained at −74.3° latitude for global biomass burning source strengths of 0, 45, and 90 Tg yr^{-1} (implying an increasing seasonal amplitude), keeping all other sources unchanged. The corresponding $\Delta\phi$ values are 165.3°, 148.2° and 138.0°. This sensitivity reflects the large $\delta^{13}C$ contrast between the relatively minor biomass burning source and the atmosphere.

To understand this behavior, we consider the effect of sources individually on the model atmosphere at latitude −74.3°. Figure 6 shows the MR and $\delta^{13}CH_4$ time series for methane produced by the animals source, taken as representative of aseasonal model sources. The MR time series has a clear seasonal cycle (with phase 199°), and the $\delta^{13}CH_4$ time series is in antiphase with it, giving a phase "ellipse" that is a straight line overlaying the KIE line. At latitude −74.3°, all the aseasonal source time series have essentially the same MR phase as that of the animals source.

Figure 7 shows the time series at −74.3° for the seasonal biomass burning source. Interestingly, MR and $\delta^{13}CH_4$ are still in antiphase. This turns out to be the case for every single-source solution (both seasonal and aseasonal), at all positions. The analytical model of *Lassey et al.* [1993] (or the work in the appendix) shows that this property holds for incremental additions and removals. Our results demonstrate that it also holds when transport is included. The biomass burning MR phase at −74.3° is significantly different from that of the animals source, being 165° compared with 199°. The seasonal swamps and bogs source time series share the same MR phase (213°), and the seasonal rice source MR phase is 232°.

Because the MR phases of the aseasonal source time series are the same, in combination their phase ellipse is essentially a straight line overlaying the KIE line. This line broadens into a phase ellipse when the seasonal sources are included. Even though the individual seasonal cycles have $\Delta\phi = 180°$ at a given position in

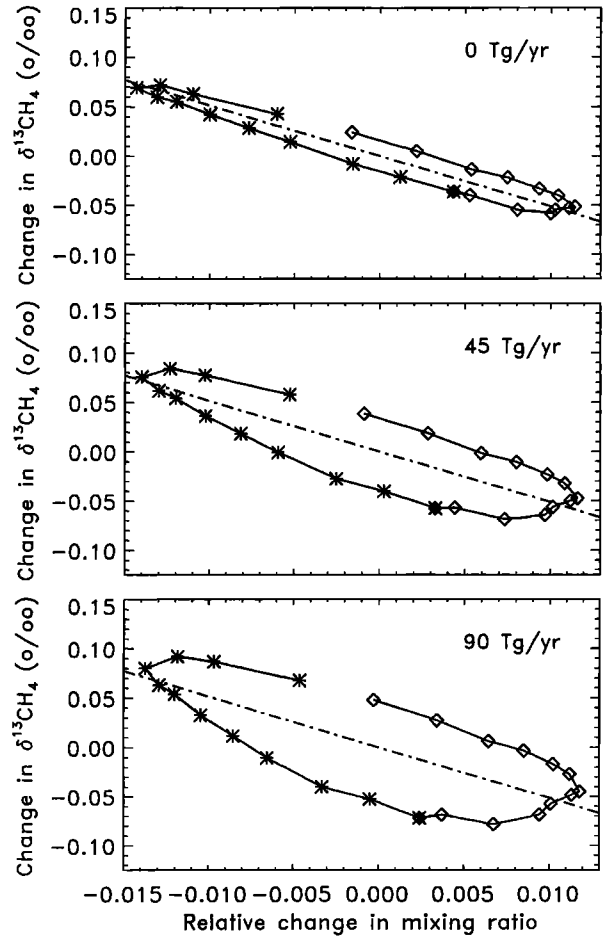

Figure 5. Modeled phase diagrams in the cell with central latitude −74.3° for global biomass burning source strengths 0, 45, and 90 Tg yr^{-1}. All other sources are unchanged. Line styles etc. are as in Figures 1e and 1f.

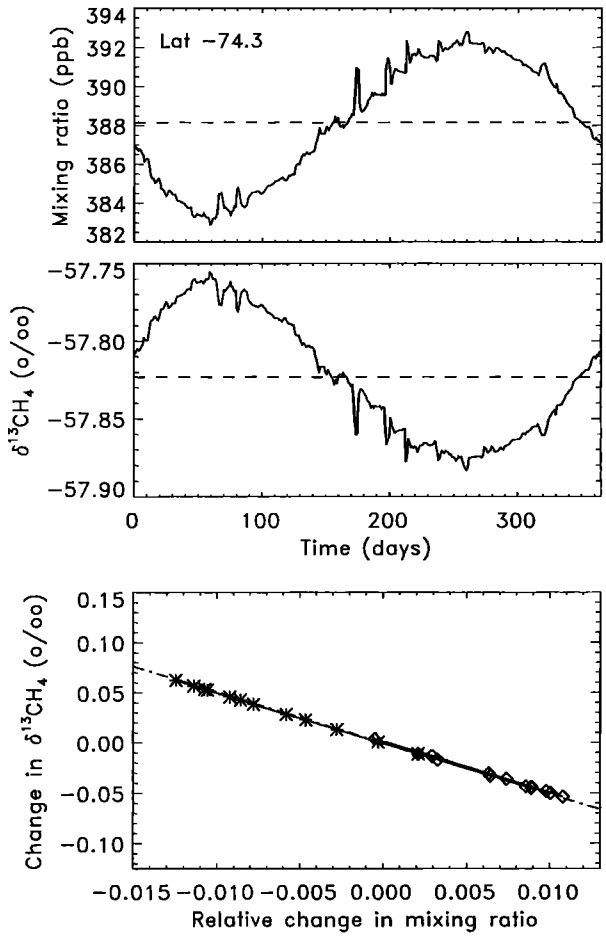

Figure 6. Modeled mixing ratio, $\delta^{13}CH_4$ and phase diagram in the cell with central latitude −74.3° for the aseasonal animals source in Table 1. Line styles etc. are as in Figures 1e and 1f.

the ETSH, when the building blocks are combined in weighted sums, the combined $\Delta\phi$ becomes significantly different from 180°. This occurs because the weights for MR are the source strengths, while the weights for $\delta^{13}CH_4$ depend strongly on the values of source $\delta^{13}C$ (see (3) and (5)). The biomass burning seasonal source has little effect on the MR seasonality (where we use "seasonality" to mean both amplitude and phase of a seasonal cycle), as it is a small component of (3) in terms of source strength. However, its different seasonal phase combined with the large contrast in its $\delta^{13}C$ compared with that of the mean source result in the biomass burning source having a relatively large effect in (5). This leads to the broadening of the ellipses in Figure 5 (bottom). The relative proximity of the biomass burning source to the ETSH is also likely to have some impact. However, a more detailed study is required to understand fully how the ETSH phase ellipses are affected by source spatial and temporal structures combined with methane transport.

In summary, while in the ETSH the length of the phase ellipse major axis is determined mainly by the sink seasonal amplitude, the eccentricity of the ellipse is determined by the seasonality of source components and the interplay between their phases and $\delta^{13}C$ contrasts. In the ETSH, the biomass burning source is the dominant contributor to the ellipse broadening because of its different seasonality combined with its large $\delta^{13}C$ contrast with the mean source.

4.4. Ellipse Major Axis Slope

The results in Figures 1 and 5 show that the slope of the phase ellipse major axis in the ETSH directly reflects the choice of the KIE, ϵ, adopted for the model atmospheric sink. Thus the adopted value of ϵ can be "estimated" by examining the orientation of the modeled phase ellipse, and this can be determined most clearly in the Antarctica / Southern Ocean region south of −65° latitude. Between −65° and about −30° latitude the slight irregularity of the ellipses makes the es-

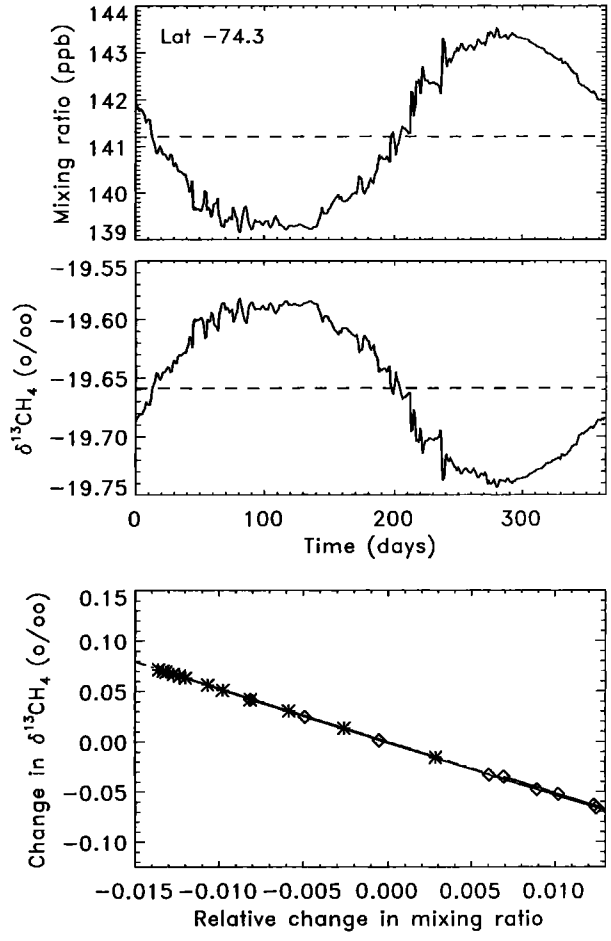

Figure 7. Modeled mixing ratio, $\delta^{13}CH_4$ and phase diagram in the cell with central latitude −74.3° for the seasonal biomass burning source in Table 1. Line styles etc. are as in Figures 1e and 1f.

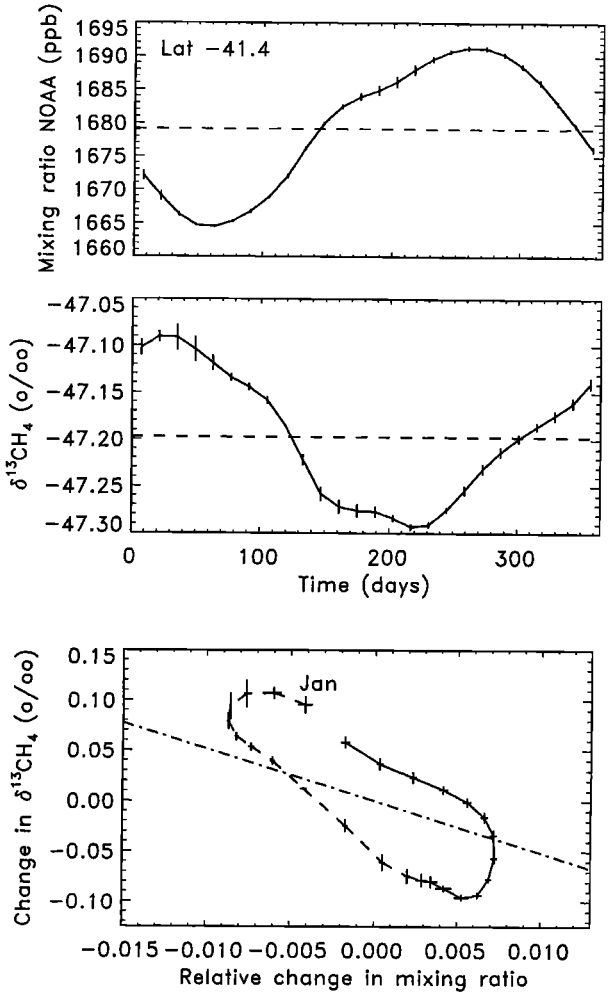

Figure 8. Mixing ratio, $\delta^{13}CH_4$, and phase diagram derived from observations at Baring Head (latitude −41.4°). Mixing ratio is reported on the National Oceanic and Atmospheric Administration (NOAA) scale [e.g., *Lang et al.*, 1992]. Smooth mean cycles have been derived as described in the text, and two-weekly averages are shown. Variability over the 4 years used in the averaging is shown by the "error" bars (2σ) at each point. In Figure 8, bottom, the first 6 months of the year are denoted by a dashed line, and the last 6 months are denoted by a solid line. The dashed-dotted line corresponds to a KIE of −5.4‰.

timate of the major axis slope somewhat less accurate. The generality of this result was supported by running a new set of building blocks with the atmospheric sink KIE changed to −10.8‰. The ellipse major axis slope increased by the amount predicted by (7). We expect therefore that a measurement-based phase ellipse in the ETSH should provide a major axis slope, particularly south of −65°, that yields a good estimate of ϵ, assuming a single atmospheric sink. North of −30° latitude the phase diagrams become so irregular that no reliable estimate of ϵ can be made.

5. Observations

In the following we compare the TM2 results with observations from the NIWA stations at Baring Head and Scott Base. For 1993–1996 the seasonal cycles have been fairly consistent from year to year, with more variability before and after that period [*Lowe et al.*, 1997; *Francey et al.*, 1999; *Lassey et al.*, 2000]. To compare the 1993–1996 observations with the TM2 model output, we determined a deseasonalized background value and a seasonal cycle from data as follows. The data for each year (selected for baseline southerly winds at Baring Head) were binned and averaged to derive 26 equally spaced points each year. In the few cases where there were missing points the loess smoothing procedure [*Cleveland and Devlin*, 1988] was applied to interpolate the missing points. The resulting data then form a regular time series to which the Seasonal-Trend-Loess (STL) procedure [*Cleveland et al.*, 1990] was applied to decompose a given time series into a long-term trend, a seasonal cycle, and an irregular component. We then determined a single mean annual cycle by averaging the

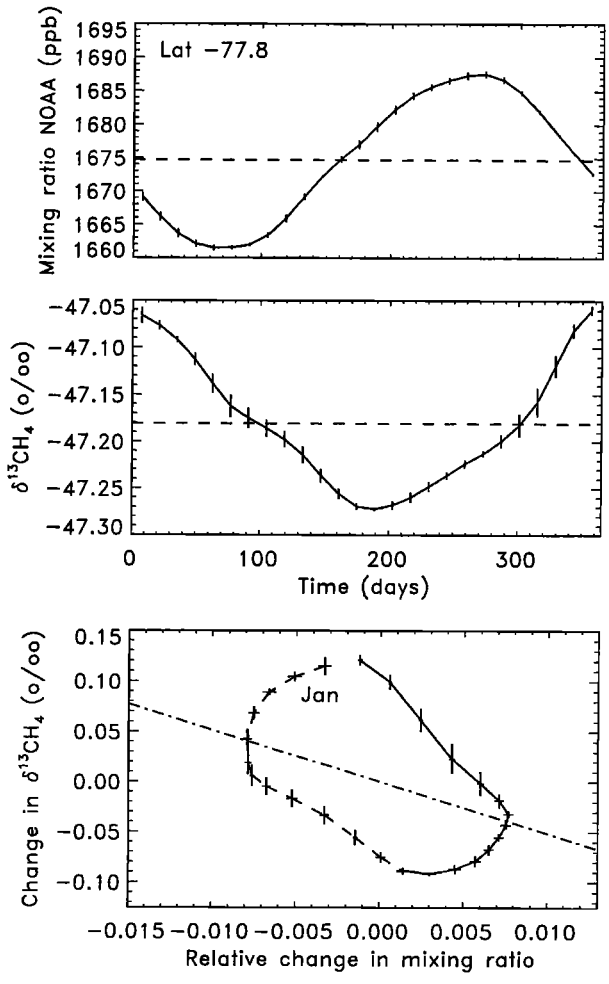

Figure 9. As Figure 8, for the observations at Scott Base (latitude −77.8°).

Table 2. Mixing Ratio and $\delta^{13}CH_4$ Amplitude, Phase, and Phase Difference From Observations at Baring Head and Scott Base Compared With TM2 Results From the Cells Containing These Stations

	A_{MR}, ppb	ϕ_{MR}, deg	A_{DC}, ‰	ϕ_{DC}, deg	$\Delta\phi$, deg
Baring Head	13.0	211.4	0.095	66.5	144.9
TM2 (−43.0°)	20.6	213.4	0.060	70.9	142.5
Scott Base	13.0	204.6	0.093	83.6	121.0
TM2 (−74.3°)	20.7	201.6	0.070	53.4	148.2

4 years 1993–1996, and added to this the mean value of the background over the 4 years. Thus we are averaging over interannual variations and assuming that disequilibrium effects and trends can be taken to be linear over the period 1993–1996.

Figures 8 and 9 show the seasonal cycles for Baring Head and Scott Base respectively. It can be seen that TM2 generates qualitatively similar MR and $\delta^{13}CH_4$ time series (Figure 1) to the observations. The observed phase ellipses have a similar January position to the modeled ellipses and the same anticlockwise rotation sense, although at Scott Base the modeled ellipse has a larger eccentricity than observed.

The parameters A_{MR} (MR amplitude), ϕ_{MR} (MR phase), A_{DC} ($\delta^{13}CH_4$ amplitude), ϕ_{DC} ($\delta^{13}CH_4$ phase), and $\Delta\phi$ were derived from the data in Figures 8 and 9. They are compared with the corresponding values from the TM2 output in Table 2. These results show that TM2 gives a good prediction of both MR and $\delta^{13}CH_4$ phases and phase difference at Baring Head using the methane budget in Table 1. This suggests that the size of the biomass burning source in Table 1 is reasonable, as this source has the largest influence on the phase difference and hence the shape of the phase ellipse. However, at both Baring Head and Scott Base, A_{MR} is overestimated by ~60%, and A_{DC} is underestimated by ~37%. We argued in section 4.1 that A_{MR} is mainly determined by the seasonal amplitude in the OH sink. A significant decrease in the modeled amplitude in the ETSH (at least from Baring Head south) appears to be required to produce the observed phase ellipse major axis. A_{DC} is locked to A_{MR} by the KIE used in the model, and together they determine the slope of the major axis as noted earlier. In confirmation of this, we were unable to adjust A_{DC} independently of A_{MR} by choosing different source strength scenarios. The effect of different source distributions has yet to be tested.

As a further test of the ellipse major axis property, we ran the simulation with an OH field modified to have 25% less OH in the ETSH than the original *Spivakovsky et al.* [1990] OH field (as Spivakovsky et al. suggested might be necessary to match ETSH observations better). The OH field was increased outside the ETSH to retain the 9-year methane lifetime. This run gave a value of A_{MR} similar to that observed at Scott Base and Baring Head. However, A_{DC} also decreased concomitantly to preserve the major axis slope at a value consistent with the sink KIE and significantly smaller than that observed. This further confirms our contention that the sink KIE robustly determines the phase ellipse tilt in the ETSH.

At Scott Base the TM2 model predicts the phase of MR well (Table 2). However, the observed phase of $\delta^{13}CH_4$ is significantly different from that predicted. This discrepancy suggests the existence of either a highly ^{13}C enriched source, or a highly fractionating sink, with appropriate seasonality in the vicinity of Scott Base. An oceanic source of methane is known but appears to be relatively small, with a $\delta^{13}C$ value probably not very different from the ambient atmosphere [e.g., *Holmes et al.*, 2000]. The larger difference in phase between MR and $\delta^{13}CH_4$ at Scott Base produces a broader ellipse. However, the ellipse major axis slopes are mutually consistent between Baring Head and Scott Base, and we now discuss the implications of this.

6. Discussion

As detailed in section 4.3, all individual sources (both seasonal and aseasonal) have phase diagrams in the ETSH that are essentially straight lines overlaid on the KIE line appropriate for destruction of methane by atmospheric OH. For MR and $\delta^{13}CH_4$ synthesized from these according to (3) and (4), we showed that differing phases of the seasonal sources can change the ellipse eccentricity in the ETSH, but this does not materially affect the ellipse major axis slope. In the model we tested various relative strengths of sources with different values of $\delta^{13}C$, for example, to simulate the source strengths of *Fung et al.* [1991] (scenario 7) and *Hein et al.* [1997] (scenario 6). In no case could we generate a phase ellipse in the ETSH with a major axis slope differing appreciably from that determined by the KIE line. We have also changed the strength and seasonal amplitude of the atmospheric sink in the ETSH significantly, with no effect on this property. As noted in section 5, A_{DC} is locked to A_{MR} by the KIE, ϵ, wherever the ellipse is sufficiently narrow. This is because the projection of the ellipse on the $\Delta\delta^{13}C$ axis is then determined by its length and major axis slope ahead

of its width. As a result, A_{MR} and A_{DC} have a common determinant, which is the seasonal amplitude of the sink strength (see section 4.1). This contrasts with the finding of *Lassey et al.* [1993] that A_{DC} in the SH is strongly influenced by the highly seasonal biomass burning source. However, that finding was in part a consequence of A_{DC} being too small to account for observation when locked by a KIE of only $-5.4‰$.

The major axis slopes of the observed phase ellipses in Figures 8 and 9 therefore appear to be inconsistent with a TM2 simulation using a KIE of $-5.4‰$ that has been measured for the OH sink. Consistency would be greatly improved by using a KIE of about $-13‰$, as also discussed by *Lowe et al.* [1999], for data collected on 1996–1997 ship transits across the Pacific. The present work, using observational data from 1993–1996, strongly supports Lowe et al.'s contention either that OH oxidation alone cannot explain the observed $\delta^{13}CH_4$ cycles or that isotope fractionation by OH in the atmosphere exceeds the laboratory measurement of $-5.4‰$ used in the model. The latter seems unlikely in the light of the lesser fractionation, $-3.9‰$, in the most recent laboratory measurement for $CH_4 + OH$ reported by *Saueressig et al.* [1999].

It is possible that stratosphere-troposphere exchange could introduce ^{13}C-rich methane into the ETSH. Using model results [e.g., *Rosenlof and Holton*, 1993] on downward mass fluxes into the ETSH from the lower stratosphere, we estimate that at most ~5% of ETSH methane may originate from stratospheric exchange. *Brenninkmeijer et al.* [1995] measured a fractionation factor of 0.988 for methane in the SH lower stratosphere, the excess over the OH fractionation factor being attributed to stratospheric removal of methane by active chlorine. Assuming uniform mixing in the ETSH, we estimate that stratospheric exchange can account for at most $-0.5‰$ of the KIE inferred at Baring Head and Scott Base. This is a minor effect compared with the discrepancy between model and observation.

As discussed by *Lowe et al.* [1999], a possible explanation for the apparently enhanced KIE is competitive removal of methane by active chlorine in the marine boundary layer (MBL). This possibility was also discussed by *Gupta et al.* [1996], and a mechanism for active chlorine production was modeled by *Vogt et al.* [1996]. There have been few estimates of active chlorine concentration, [Cl], in the ETSH MBL. From nonmethane hydrocarbon observations in the MBL south of Australia, *Wingenter et al.* [1999] inferred an average [Cl] of $720\,cm^{-3}$ in early spring. An aseasonal active chlorine sink would not change the inferred KIE from the OH value of $-5.4‰$. However, it seems probable from observations of halide loss from sea-salt particles [e.g., *Ayers et al.*, 1999] that there is an appreciable seasonal cycle of active chlorine in this region, with a maximum in summer. Because it is linked to incident radiation, such a cycle could qualitatively resemble the OH seasonal cycle given by *Spivakovsky et al.* [1990].

To estimate the effect of a seasonal active chlorine cycle on $\delta^{13}CH_4$, we developed a simple chemical box model of methane destruction in the ETSH MBL by both OH (with KIE $-5.4‰$) and active chlorine. We assumed that active chlorine has a similar form of seasonal cycle to that of OH and that the winter minimum [Cl] was $600\,cm^{-3}$. Using a $CH_4 + Cl$ KIE of $-66‰$ [*Saueressig et al.*, 1995; *Crowley et al.*, 1999; *Tyler et al.*, 2000], we determined the elevated [Cl] necessary during summer to give an effective KIE of $-13‰$ measured from the slope of the KIE line. The seasonal peak [Cl] was $6.3 \cdot 10^3\,cm^{-3}$, with a yearly average of $3.5 \cdot 10^3\,cm^{-3}$, a value in the middle of the range discussed in the modeling study by *Vogt et al.* [1996]. If this average value of [Cl] applied over the global ocean, then the MBL global active chlorine sink strength would be $< 5\,Tg\,yr^{-1}$. Details of this study will be presented elsewhere.

7. Conclusions

We have derived the spatial and temporal variation of $\delta^{13}C$ in atmospheric methane using the TM2 atmospheric tracer model with 1987 wind fields and a methane source budget based on recent literature. Our conclusions from analysis of the model output and comparison with observations at Baring Head and Scott Base are as follows.

1. The TM2 results in the ETSH show MR and $\delta^{13}CH_4$ seasonalities that are qualitatively similar to those observed. The seasonal cycles are smooth enough, particularly over the Southern Ocean, that clear phase ellipses are obtained when changes in $\delta^{13}CH_4$ are plotted versus changes in MR. Outside the ETSH, temporal variability is so large that phase ellipses are generally not apparent.

2. In the ETSH, the modeled ellipse major axis slope is a very good measure of the kinetic isotope effect (ϵ) that characterizes the single atmospheric sink used in the model. This appears to be a robust property. However, the ϵ implied by phase ellipses that are based on observations at Baring Head and Scott Base is a factor of 2 – 4 larger than values based on laboratory measurements of the OH KIE by *Cantrell et al.* [1990] and *Saueressig et al.* [1999].

3. The eccentricity of the phase ellipse is determined by the phase difference between MR and $\delta^{13}CH_4$ cycles. This in turn is dominantly determined in the ETSH by the biomass burning source because of its high ^{13}C enrichment and strong seasonal amplitude. The ellipse eccentricities observed at Baring Head and Scott Base show differences that are not predicted by the model.

4. The ellipse major axis length is fixed by the amplitude of the MR seasonality, which is dominantly determined by the OH sink seasonal amplitude. Our TM2 results overestimate the MR seasonal amplitude by ~60%, suggesting that the seasonal amplitude in the OH sink used is too large. This is partly explained

by our strengthening of the OH fields of *Spivakovsky et al.* [1990] using a constant multiplier of 1.278, in order to achieve the observed methane lifetime (see section 2). This has the effect of increasing the OH seasonal amplitude by ~28%, reinforcing the observation by *Spivakovsky et al.* [1990] that their OH field (without strengthening) already overestimated by 33% the CH_3CCl_3 seasonal amplitude south of about −20° latitude.

The discrepancies between model results and observations described in points 2 and 3 suggest the existence of either a highly ^{13}C enriched methane source or a highly fractionating methane sink (or possibly both together). The sink is consistent with methane destruction by active chlorine in the MBL, provided the concentration of active chlorine there has an appreciable seasonal cycle. Preliminary estimates suggest that the modeled yearly mean active chlorine concentration is consistent with other modeling studies and would correspond to a methane sink of order 5 Tg yr^{-1}.

Appendix: The KIE Line

Consider a closed well-mixed box with methane burden C_n of isotope $^nCH_4$ and combined burden C. Then

$$C = C_{12} + C_{13} \quad (8)$$

$$C_{13}/C_{12} = R_0(1+\delta), \quad (9)$$

where $\delta \equiv \delta^{13}CH_4$. Consider separately small changes to methane in the box that are driven by a single first-order removal process and by an aggregate methane source. Seasonal or similar variations can then be thought of as driven by a succession or superposition of such incremental sink and source processes.

Consider first methane removal that discriminates between the isotopes resulting in a fractionated residual methane. The $^nCH_4$ removal rate is λ_n, and the fractionation factor $\alpha = 1+\epsilon$ is therefore $\lambda_{13}/\lambda_{12}$. The rate of $^nCH_4$ removal is

$$\partial C_n/\partial t = -\lambda_n C_n.$$

We can therefore write

$$\frac{\Delta C_{13}}{\Delta C_{12}} = \frac{\lambda_{13}}{\lambda_{12}}\frac{C_{13}}{C_{12}}, \quad (10)$$

where small removals ΔC_n occur over a short time Δt. From (9) and (10)

$$\Delta C_{13} = R_0(1+\epsilon)(1+\delta)\Delta C_{12}. \quad (11)$$

By differentiating (9), small changes ΔC_{12}, ΔC_{13} are interrelated to small changes $\Delta\delta$ in δ through

$$\Delta C_{13} = R_0[(1+\delta)\Delta C_{12} + C_{12}\Delta\delta]. \quad (12)$$

Solving (11) and (12) for ΔC_{12} and ΔC_{13} and substituting into $\Delta C = \Delta C_{12} + \Delta C_{13}$ (from (8)) gives an expression for $\Delta\delta$ in terms of ΔC

$$\Delta\delta = \epsilon(1+\delta)\left[\frac{1+R_0(1+\delta)}{1+\alpha R_0(1+\delta)}\right]\frac{\Delta C}{C}. \quad (13)$$

Therefore we can take

$$\Delta\delta \approx \epsilon(1+\delta_0)\Delta C/C_0, \quad (14)$$

neglecting terms of order $\epsilon\Delta C/C$ and ϵR_0 compared with unity, δ_0 and C_0 being the mean values of δ and C over the short time interval Δt.

We next consider methane changes in the box driven by an incremental methane source S with $\delta^{13}CH_4$ value δ_S corresponding to isotopic components S_{12} and S_{13}. Then the accumulation rate of $^nCH_4$ in the box is

$$\partial C_n/\partial t = S_n$$

so that the analogue of (10) is

$$\frac{\Delta C_{13}}{\Delta C_{12}} = \frac{S_{13}}{S_{12}} = R_0(1+\delta_S). \quad (15)$$

This leads to the source counterpart of (13) as

$$\Delta\delta = (\delta_S - \delta)\left[\frac{1+R_0(1+\delta)}{1+R_0(1+\delta_S)}\right]\frac{\Delta C}{C}. \quad (16)$$

If successive sink and source increments maintain variation about an equilibrium state, then δ_S will be related to δ and ϵ through (6), namely $\delta_S = \alpha\delta + \epsilon$. When this relationship is imposed, (13) and (16) are exactly equivalent. Thus, for relatively small sink and source variations about equilibrium, variations $\Delta\delta$ in δ are related linearly to variations $\Delta C/C_0$ in methane burden (or MR) to first order through (14). We term this relationship the "KIE line," with slope $\epsilon(1+\delta_0)$ that is independent of mean source strength and removal rate.

Acknowledgments. We thank the referees for constructive comments that have improved this paper. We thank Martin Heimann for providing us with the TM2 tracer model and Peter Bergamaschi for useful comments on the manuscript. This work was supported by the New Zealand Foundation for Research, Science and Technology through contracts C01826 and C01X0034.

References

Ayers, G. P., R. W. Gillett, J. M. Cainey, and A. L. Dick, Chloride and bromide loss from sea-salt particles in Southern Ocean air, *J. Atmos. Chem., 33,* 299–319, 1999.

Bergamaschi, P., M. Braunlich, T. Marik, and C. A. M. Brenninkmeijer, Measurements of the carbon and hydrogen isotopes of atmospheric methane at Izana, Tenerife: Seasonal cycles and synoptic-scale variations, *J. Geophys. Res., 105,* 14,531–14,546, 2000.

Brenninkmeijer, C. A. M., D. C. Lowe, M. R. Manning, R. J. Sparks, and P. F. J. van Velthoven, The ^{13}C, ^{14}C, and ^{18}O isotopic composition of CO, CH_4, and CO_2 in the higher southern latitudes lower stratosphere, *J. Geophys. Res., 100,* 26,163–26,172, 1995.

Cantrell, C. A., et al., Carbon kinetic isotope effect in the oxidation of methane by the hydroxyl radical, *J. Geophys. Res., 95*, 22,455–22,462, 1990.

Cleveland, R. B., W. S. Cleveland, J. E. McRae, and I. Terpenning, STL: A seasonal-trend decomposition procedure based on loess, *J. Off. Stat. (Stat. Sweden), 6*, 3–73, 1990.

Cleveland, W. S., and S. J. Devlin, Locally-weighted regression: An approach to regression analysis by local fitting, *J. Am. Stat. Assoc., 83*, 596–610, 1988.

Craig, H., Isotopic standards for carbon and oxygen and correction factors for mass spectrometric analysis of carbon dioxide, *Geochim. Cosmochim. Acta, 12*, 133–149, 1957.

Crowley, J. N., G. Saueressig, P. Bergamaschi, H. Fischer, and G. W. Harris, Carbon kinetic isotope effect in the reaction CH_4 + Cl: A relative rate study using FTIR spectroscopy, *Chem. Phys. Lett., 303*, 268–274, 1999.

Crutzen, P. J., The role of methane in atmospheric chemistry and climate, in *Ruminant Physiology: Digestion, Metabolism, Growth and Reproduction: Proceedings 8th International Symposium on Ruminant Physiology*, edited by W. von Engelhardt et al., pp. 291–315, Ferdinand Enke Verlag, Stuttgart, Germany, 1995.

DeMore, W. B., et al., Chemical kinetics and photochemical data for use in stratospheric modeling – Evaluation Number 12, *Publ. 97-4*, Jet Propulsion Lab., Pasadena, Calif., 1997.

Denning, A. S., et al., Three-dimensional transport and concentration of SF_6: A model intercomparison study (TransCom 2), *Tellus, Ser. B, 51*, 266–297, 1999.

Etheridge, D. M., L. P. Steele, R. J. Francey, and R. L. Langenfelds, Atmospheric methane between 1000 A.D. and present: Evidence of anthropogenic emissions and climatic variability, *J. Geophys. Res., 103*, 15,979–15,993, 1998.

Francey, R. J., et al., A history of $\delta^{13}C$ in atmospheric CH_4 from the Cape Grim Air Archive and Antarctic firn air, *J. Geophys. Res., 104*, 23,631–23,643, 1999.

Fung, I., et al., Three-dimensional model synthesis of the global methane cycle, *J. Geophys. Res., 96*, 13,033–13,065, 1991.

Gupta, M., S. Tyler, and R. Cicerone, Modeling atmospheric $\delta^{13}CH_4$ and the causes of recent changes in atmospheric CH_4 amounts, *J. Geophys. Res., 101*, 22,923–22,932, 1996.

Heimann, M., The global atmospheric tracer model TM2, *Tech. Rep. 10*, Deutsches Klimarechenzentrum, Hamburg, Germany, 1995.

Heimann, M., and C. D. Keeling, A three-dimensional model of atmospheric CO_2 transport based on observed winds, 2, Model description and simulated tracer experiments, in *Aspects of Climate Variability in the Pacific and the Western Americas*, Geophys. Monogr. Ser., vol. 55, edited by D. H. Peterson, pp. 237–275, AGU, Washington, DC, 1989.

Hein, R., P. J. Crutzen, and M. Heimann, An inverse modelling approach to investigate the global atmospheric methane cycle, *Global Biogeochem. Cycles, 11*, 43–76, 1997.

Holmes, M. E., F. J. Sansone, T. M. Rust, and B. N. Popp, Methane production, consumption, and air-sea exchange in the open ocean: An evaluation based on carbon isotope ratios, *Global Biogeochem. Cycles, 14*, 1–10, 2000.

Houweling, S., F. Dentener, and J. Lelieveld, The impact of nonmethane hydrocarbon compounds on tropospheric chemistry, *J. Geophys. Res., 103*, 10,673–10,696, 1998.

Keeling, C. D., et al., A three-dimensional model of atmospheric CO_2 transport based on observed winds, 1, Analysis of observational data, in *Aspects of Climate Variability in the Pacific and the Western Americas*, Geophys. Monogr. Ser., vol. 55, edited by D. H. Peterson, pp. 165–236, AGU, Washington, DC, 1989.

Lang, P. M., et al., *NOAA/CMDL Atmospheric Methane Data for the Period 1983–1990 From Shipboard Flask Samples, Rep. ERL CMDL-4*, Nat. Oceanic and Atmos. Admin., Boulder, Colo., 1992.

Lassey, K. R., D. C. Lowe, C. A. M. Brenninkmeijer, and A. J. Gomez, Atmospheric methane and its carbon isotopes in the southern hemisphere: Their time series and an instructive model, *Chemosphere, 26*, 95–109, 1993.

Lassey, K. R., D. C. Lowe, and M. R. Manning, The trend in atmospheric methane $\delta^{13}C$ and implications for isotopic constraints on the global methane budget, *Global Biogeochem. Cycles, 14*, 41–49, 2000.

Lowe, D. C., et al., Concentration and ^{13}C records of atmospheric methane in New Zealand and Antarctica: Evidence for changes in methane sources, *J. Geophys. Res., 99*, 16,913–16,925, 1994.

Lowe, D. C., M. R. Manning, G. W. Brailsford, and A. M. Bromley, The 1991–1992 atmospheric methane anomaly: Southern hemisphere ^{13}C decrease and growth rate fluctuations, *Geophys. Res. Lett., 24*, 857–860, 1997.

Lowe, D. C., et al. Shipboard determinations of the distribution of ^{13}C in atmospheric methane in the Pacific, *J. Geophys. Res., 104*, 26, 125-26, 135, 1999.

Prather, M., R. Derwent, D. Ehhalt, P. Fraser, E. Sanhueza, and X. Zhou, Other trace gases and atmospheric chemistry, in *Climate Change 1994: Radiative Forcing of Climate Change*, edited by J. T. Houghton et al., pp. 73–126, Cambridge Univ. Press, New York, 1995.

Prinn, R. G., et al., Atmospheric trends and lifetime of CH_3CCl_3 and global OH concentrations, *Science, 269*, 187–192, 1995.

Quay, P. D., et al., Carbon isotopic composition of atmospheric CH_4: Fossil and biomass burning source strengths, *Global Biogeochem. Cycles, 5*, 25–47, 1991.

Quay, P. D., J. Stutsman, D. Wilbur, A. Snover, E. Dlugokencky, and T. Brown, The isotopic composition of atmospheric methane, *Global Biogeochem. Cycles, 13*, 445–461, 1999.

Rosenlof, K. H., and J. R. Holton, Estimates of the stratospheric residual circulation using the downward control principle, *J. Geophys. Res., 98*, 10,465–10,479, 1993.

Saueressig, G., P. Bergamaschi, J. N. Crowley, H. Fischer, and G. W. Harris, Carbon kinetic isotope effect in the reaction of CH_4 with Cl atoms, *Geophys. Res. Lett., 22*, 1225–1228, 1995.

Saueressig, G., P. Bergamaschi, J. N. Crowley, C. Brühl, and H. Fischer, Carbon and hydrogen kinetic isotope effects (KIE) of methane in its atmospheric chemical sink processes: New results for the reaction CH_4+OH (abstr.), Eur. Geophys. Soc., The Hague, 1999.

Schimel, D., et al., Radiative forcing of climate change, in *Climate Change 1995: The Science of Climate Change*, edited by J. T. Houghton, et al., pp. 67–131, Cambridge Univ. Press, New York, 1996.

Snover, A. K., and P. D. Quay, Hydrogen and carbon kinetic isotope effects during soil uptake of atmospheric methane, *Global Biogeochem. Cycles, 14*, 25–39, 2000.

Spivakovsky, C. M., R. Yevich, J. A. Logan, S. C. Wofsy, and M. B. McElroy, Tropospheric OH in a three-dimensional chemical tracer model: An assessment based on observations of CH_3CCl_3, *J. Geophys. Res., 95*, 18,441–18,471, 1990.

Stevens, C. M., and A. Engelkemeir, Stable carbon isotopic composition of methane from some natural and anthropogenic sources, *J. Geophys. Res., 93*, 725–733, 1988.

Tans, P. P., A note on isotopic ratios and the global atmospheric methane budget, *Global Biogeochem. Cycles, 11*, 77–81, 1997.

Tyler, S. C., P. M. Crill, and G. W. Brailsford, $^{13}C/^{12}C$ fractionation of methane during oxidation in a temperate forested soil, *Geochim. Cosmochim. Acta, 58,* 1625–1633, 1994.

Tyler, S. C., H. O. Ajie, A. L. Rice, R. J. Cicerone, and E. C. Tuazon, Experimentally determined kinetic isotope effects in the reaction of CH_4 with Cl: Implications for atmospheric CH_4, *Geophys. Res. Lett., 27,* 1715–1718, 2000.

Vogt, R., P. J. Crutzen, and R. Sander, A mechanism for halogen release from sea-salt aerosol in the remote marine boundary layer, *Nature, 383,* 327–329, 1996.

Wingenter, O. W., et al., Tropospheric hydroxyl and atomic chlorine concentrations, and mixing timescales determined from hydrocarbon and halocarbon measurements made over the Southern Ocean, *J. Geophys. Res., 104*, 21,819–21,828, 1999.

W. Allan, A. J. Gomez, K. R. Lassey, D. C. Lowe, and M. R. Manning, NIWA, Brodie Building, 301 Evans Bay Parade, P. O. Box 14-901, Kilbirnie, Wellington 6003, New Zealand. (w.allan@niwa.cri.nz)

(Received March 24, 2000; revised October 10, 2000; accepted October 31, 2000.)